HHS Public Access

Author manuscript

J Am Chem Soc. Author manuscript; available in PMC 2018 April 16.

Published in final edited form as:

J Am Chem Soc. 2017 December 20; 139(50): 18295–18306. doi:10.1021/jacs.7b09937.

Unusual Role of Excited State Mixing in the Enhancement of Photoinduced Ligand Exchange in Ru(II) Complexes

Lauren M. Loftus[†], **Ao Li**[‡], **Kathlyn L. Fillman**[†], **Philip D. Martin**[‡], **Jeremy J. Kodanko**[‡,*], and **Claudia Turro**[†,*]

[†]Department of Chemistry and Biochemistry, The Ohio State University, Columbus, Ohio 43210, United States

[‡]Department of Chemistry, Wayne State University, Detroit, Michigan 48202, United States

Abstract

Four Ru(II) complexes were prepared bearing two new tetradentate ligands, cyTPA and 1-isocyTPQA, which feature a piperidine ring that provides a structurally rigid backbone and facilitates the installation of other donors as the fourth chelating arm, while avoiding the formation of stereoisomers. The photophysical properties and photochemistry of [Ru(cyTPA)$(CH_3CN)_2]^{2+}$ (**1**), [Ru(1-isocyTPQA)$(CH_3CN)_2]^{2+}$ (**2**), [Ru(cyTPA)$(py)_2]^{2+}$ (**3**), and [Ru(1-isocyTPQA)-$(py)_2]^{2+}$ (**4**) were compared. The quantum yield for the CH_3CN/H_2O ligand exchange of **2** was measured to be Φ_{400} = 0.033(3), 5-fold greater than that of **1**, Φ_{400} = 0.0066(3). The quantum yields for the py/H_2O ligand exchange of **3** and **4** were lower, 0.0012(1) and 0.0013(1), respectively. DFT and related calculations show the presence of a highly mixed ^{3}MLCT/$^3\pi\pi^*$ excited state as the lowest triplet state in **2**, whereas the lowest energy triplet states in **1**, **3**, and **4** were calculated to be ^{3}LF in nature. The mixed ^{3}MLCT/$^3\pi\pi^*$ excited state places significant spin density on the quinoline moiety of the 1-isocyTPQA ligand positioned *trans* to the photolabile CH_3CN ligand in **2**, suggesting the presence of a *trans*-type influence in the excited state that enhances ligand exchange. Ultrafast spectroscopy was used to probe the excited states of **1–4**, which confirmed that the mixed ^{3}MLCT/$^3\pi\pi^*$ excited state in **2** promotes ligand dissociation, representing a new manner to effect photoinduced ligand exchange. The findings from this work can be used to design improved complexes for applications that require efficient ligand dissociation, as well as for those that require minimal deactivation of the ^{3}MLCT state through low-lying metal-centered states.

[*]Corresponding Authors: jkodanko@chem.wayne.edu, turro.1@osu.edu.

ORCID

Jeremy J. Kodanko: 0000-0001-5196-7463

Claudia Turro: 0000-0003-3202-5870

ASSOCIATED CONTENT

Supporting Information

The Supporting Information is available free of charge on the ACS Publications website at DOI: 10.1021/jacs.7b09937. Structural characterization data for ligands and complexes **1–4**, X-ray crystallographic data for **1–3**, electronic absorption data for **3–4**, dark controls, ^{1}H NMR photolysis of **1–2**, experimental and calculated bond lengths and frequencies, TD-DFT energies and assignments, optimized ground and excited state atomic coordinates, charge decomposition analysis, calculated molecular orbital energy diagrams, experimental setup of transient absorption spectrometer, and additional experimental and simulated transient absorption data (PDF)

Notes

The authors declare no competing financial interest.

Graphical Abstract

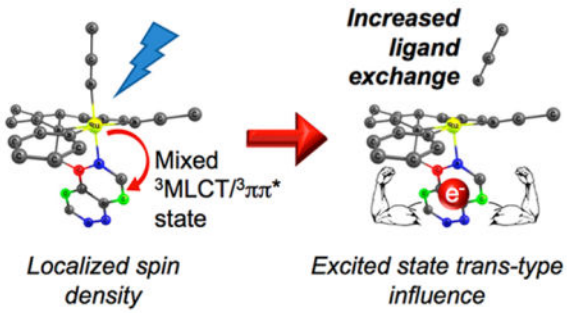

INTRODUCTION

The excited states of ruthenium polypyridyl complexes have been used extensively in the areas of dye-sensitized solar cells, photocatalysis, synthetic chemistry, photochromic switching, photochemotherapy, and as biological sensors, among others.[1–32] The utility of these complexes for these applications relies on their relatively strong absorption and emission intensity in the visible region, long-lived triplet metal-to-ligand charge transfer (^{3}MLCT) excited state lifetimes, and high stability under various experimental conditions.[1–33] In contrast, the efficient photoinduced ligand dissociation for the release of drugs or biological probes with spatiotemporal control necessitates the population of the dissociative metal-centered, ligand field states (^{3}LF), known to lead to nonradiative deactivation of the emissive ^{3}MLCT state.[14,34–41] Therefore, understanding the interplay between the ^{3}MLCT and ^{3}LF states is important to improve the function of Ru(II) complexes, both when the long-lived ^{3}MLCT state is desired, as well as for cases where increased ^{3}LF population is required.[14,42] Therefore, the improvement of agents for this wide range of applications requires understanding of the molecular and electronic factors that result in ^{3}MLCT deactivation and ligand photodissociation through population of the ^{3}LF state(s).

The excited state ligand exchange photochemistry of Ru(II) complexes has long been believed to arise from ^{3}LF states with electron configurations that result in electron density in molecular orbitals of Ru–L(σ^*) character.[14] In complexes with low-lying ^{3}MLCT and ^{3}LF states, such as in ruthenium polypyridyl compounds, it is generally accepted that those with lower energy ^{3}LF states should exhibit greater ligand photo-dissociation quantum yields.[14,27,30,39,42–44] This trend was shown by Ford and co-workers on the series $[Ru(NH_3)_5(py\text{-}X)]^{2+}$ (py-X = substituted pyridine) and *trans*-$[Ru(NH_3)_4(py)\text{-}(L)]^{n+}$ (py = pyridine; L = pyrazine, pyrazinium, 4-acetylpyridine), which resulted in quantum yields of ligand substitution that spanned over 3 orders of magnitude.[45] The incorporation of electron donating substituents on pyridine led to mainly ^{3}LF character in the lowest triplet excited states and efficient photosubstitution, whereas electron withdrawing substituents resulted in mostly ^{3}MLCT character and decreased photosubstitution efficiency.[34,45,46] In addition, it has been shown that in complexes where the ^{3}MLCT state remains the lowest energy triplet state, reducing the ^{3}MLCT–^{3}LF energy gap by either raising the ^{3}MLCT state or lowering the ^{3}LF state, can also lead to increased population of the dissociative ^{3}LF states.[39,47–50] On the basis of this understanding of photoinduced ligand dissociation in Ru(II) polypyridyl

complexes, it follows that the photochemical ligand exchange should be more efficient in complexes where the lowest energy excited state is metal-centered, ^{3}LF, and not ^{3}MLCT. The latter condition should hold provided that the energy of the ^{3}LF states are not so low that intersystem crossing back to the ground state becomes too rapid and competes with ligand dissociation in accordance with the energy gap law.[44,50]

The majority of studies concerning the photochemical ligand exchange of polypyridyl Ru(II) complexes have focused on complexes containing planar bi- or tridentate ligands, such as the prototypical 2,2′-bipyridine or 2,2′:6′,2″-terpyridine, respectively, and their derivatives.[27,41,48,51–55] Recently, the photochemistry of Ru(II) complexes bearing tetradentate ligands based on tris(2-pyridylmethyl)amine (TPA) was examined. In both $[Ru(TPA)(CH_3CN)_2]^{2+}$ and $[Ru(TPA)\text{-}(py)_2]^{2+}$, the monodentate ligand *cis* to the basic amine nitrogen of the TPA ligand was shown to undergo preferential ligand photodissociation, with quantum yields (**Φ**) in H_2O of 0.012(1) with λ_{irr} = 350 nm and 0.0097(8) with λ_{irr} = 400 nm, respectively.[56,57] The photochemistry of a related nitrile complex containing the tetradentate ligand tris(2-quinolinylmethyl)amine (TQA), $[Ru(TQA)(CH_3CN)_2]^{2+}$, resulted in Φ_{400} = 0.027(1) in H_2O, ~2-fold greater than that of $[Ru(TPA)(CH_3CN)_2]^{2+}$. Like $[Ru(TPA)(CH_3CN)_2]^{2+}$ and $[Ru(TPA)(py)_2]^{2+}$, irradiation of $[Ru(TQA)(CH_3CN)_2]^{2+}$ only results in ligand exchange of the CH_3CN positioned *cis* to the basic amine nitrogen of the TQA ligand.[58] Calculations provided an explanation for the increase and selectivity of ligand exchange, showing the presence of favorable orbital overlap in the excited state between the coplanar quinoline arms of the TQA ligand and the photolabile CH_3CN ligand that is not present in the TPA complex.[59]

In the present work, four new Ru(II) complexes were prepared bearing two new tetradentate ligands related to TPA, cyTPA (2,2′-((2*R*,6*S*)-1-(pyridin-2-ylmethyl)piperidine-2,6-diyl)dipyridine) and 1-isocyTPQA (1-(((2*R*,6*S*)-2,6-di-(pyridin-2-yl)piperidin-1-yl)methyl)isoquinoline), depicted in Figure 1. These ligands feature a piperidine ring, which locks the adjacent pyridine arms into the *trans* position to form a planar tridentate moiety within the tetradentate ligand. This structurally rigid backbone facilitates the installation of other donors as the fourth chelating arm, while avoiding the formation of stereoisomers. The photophysical properties and photochemistry of $[Ru(cyTPA)(CH_3CN)_2]^{2+}$ (**1**) and [Ru(1-isocyTPQA)$(CH_3CN)_2]^{2+}$ (**2**) were compared, as well as to those of the corresponding pyridine complexes, $[Ru(cyTPA)\text{-}(py)_2]^{2+}$ (**3**) and $[Ru(1\text{-}isocyTPQA)(py)_2]^{2+}$ (**4**). Photo-induced ligand exchange was found to be significantly more efficient for **2**, a property that was investigated using ultrafast transient absorption spectroscopy and computational studies. The findings provide a new mechanism that leads to ligand dissociation that does not involve a low-lying ^{3}LF state and can now be exploited in the design of new complexes for efficient photoinduced drug delivery with low energy excitation. These results also provide insight into an additional mode of deactivation of Ru(II) complexes important for solar energy conversion applications and the use of these systems as emissive probes, all of which require long-lived ^{3}MLCT excited states and minimum deactivation through nonradiative channels.

EXPERIMENTAL SECTION

Materials

All materials for synthesis were used as received without further purification and the solvents were of reagent grade quality. Dry methanol, absolute ethanol, dry acetonitrile, acetone, ethyl acetate, dichloromethane, hexane, dimethyl sulfoxide (DMSO), diethyl ether and pyridine were purchased from Fisher Scientific. Trifluoromethanesulfonic acid, 2-picolyl chloride hydrochloride, *N*,*N*-diisopropylethylamine (DIPEA), and tetrakis(dimethyl sulfoxide)-dichlororuthenium(II) (*cis*-$[Ru(DMSO)_4Cl_2]$) were purchased from Sigma-Aldrich. Ammonium hexafluorophosphate was obtained from AK Scientific, and $NaI{\cdot}2H_2O$ was purchased from ACROS Organics. The precursors (2*R*,6*S*)-2,6-di(pyridin-2-yl)piperidine[60] and 1-(chloromethyl)isoquinoline[61] were synthesized according to literature procedures. All reactions were performed under ambient atmosphere unless otherwise noted. Anaerobic reactions were performed by purging the reaction solutions with Ar or N_2. For transient absorption experiments acetone was dried using anhydrous $MgSO_4$, and acetonitrile was distilled over CaH_2.

cyTPA (2,2′-((2R,6S)-1-(pyridin-2-ylmethyl)piperidine-2,6-diyl)-dipyridine)—To a solution of (2*R*,6*S*)-2,6-di(pyridin-2-yl)piperidine (36 mg, 0.15 mmol) in 11 mL of dry CH_3CN, 2-picolyl chloride hydrochloride (25 mg, 0.15 mmol) was added. To this, DIPEA (52 μL, 0.30 mmol) and $NaI{\cdot}2H_2O$ (28 mg, 0.15 mmol) were added and the reaction mixture was heated at 50 °C for 16 h. The reaction mixture was cooled to room temperature and concentrated under reduced pressure, and the residue was extracted with dichloromethane and an aqueous solution of saturated $NaHCO_3$. The organic layer was concentrated under reduced pressure to give the crude product, which was purified by chromatography on silica using ethyl acetate as the eluent to give cyTPA as a yellow solid (26 mg, 52%): ^{1}H NMR (400 MHz, $CDCl_3$) δ 8.46 (d, 2H, J = 4.8 Hz), 8.18 (d, 1H, J = 4.8 Hz), 7.57 (d, 2H, J = 8.0 Hz), 7.50 (t, 2H, J = 7.6 Hz), 7.31 (t, 1H, J = 7.6 Hz), 7.04–7.00 (m, 3H), 6.84 (t, 1H, J = 6.0 Hz), 3.86 (d, 2H, J = 9.6 Hz), 3.63 (s, 2H), 1.90–1.81 (m, 4H), 1.64–1.58 (m, 2H); ^{13}C NMR (600 MHz, $CDCl_3$) δ 163.7, 159.4, 148.8, 148.1, 136.2, 135.1, 123.8, 123.0, 122.0, 120.8, 70.2, 59.6, 34.8, 24.3; ESMS calculated for ($[M + H]^+$) $C_{21}H_{23}N_4$: 331.1878, found ($[M + H]^+$): 331.1919.

1-IsocyTPQA (1-(((2R,6S)-2,6-di(pyridin-2-yl)piperidin-1-yl)-methyl)isoquinoline)—To a solution of (2*R*,6*S*)-2,6-di(pyridin-2-yl)piperidine (20 mg, 0.084 mmol) in 6.0 mL of dry CH_3CN, 1-(chloromethyl)isoquinoline (15 mg, 0.084 mmol) was added. To this, DIPEA (29 μL, 0.17 mmol) and $NaI{\cdot}2H_2O$ (16 mg, 0.084 mmol) were added and the reaction mixture was heated at 50 °C for 16 h. The reaction mixture was cooled to room temperature and concentrated under reduced pressure, and the residue was extracted with dichloromethane and an aqueous solution of saturated $NaHCO_3$. The organic layer was dried over Na_2SO_4 and concentrated under reduced pressure to give the crude product, which was purified by chromatography on silica using methanol/ethyl acetate (1:9, v/v) as the eluent to give 1-isocyTPQA as an orange solid (15 mg, 47%): ^{1}H NMR (500 MHz, CD_3OD) δ 8.19–8.15 (m, 3H), 7.92 (d, 1H, J = 8.5 Hz), 7.67 (d, 1H, J = 8.0 Hz), 7.62 (d, 3H, J = 7.5 Hz), 7.52–7.46 (m, 3H), 7.39 (s, 1H), 7.02–6.99 (m, 2H), 4.09 (s, 2H), 4.03

(dd, 2H, J = 10 Hz), 1.95–1.83 (m, 4H), 1.73–1.70 (m, 2H); ^{13}C NMR (500 MHz, CD_3OD) δ 163.0, 157.9, 147.6, 139.4, 136.7, 135.9, 130.2, 126.9, 126.8, 126.6, 125.4, 123.3, 122.1, 120.3, 70.1, 54.5, 34.6, 23.7; ESMS calculated for $C_{25}H_{25}N_4$ ($[M + H]^+$): 381.2079, found ($[M + H]^+$): 381.1794.

[Ru(cyTPA)(CH$_3$CN)$_2$](PF$_6$)$_2$ (*1*)—To a solution of cyTPA (13 mg, 0.040 mmol) in 4.0 mL of dry MeOH under inert atmosphere in a pressure flask, *cis*-$[Ru(DMSO)_4Cl_2]$ (19 mg, 0.040 mmol) was added. The solution was then purged with Ar for 10 min at room temperature, and the reaction mixture was allowed to reflux for 5 h under inert atmosphere, during which time the color of the reaction mixture darkened slightly. The reaction mixture was cooled to room temperature and concentrated under reduced pressure. To the flask, a mixture of CH_3CN:H_2O (1:1 v/v, 4.0 mL) was added, and the reaction mixture was refluxed for another 16 h under inert atmosphere. The reaction mixture was again cooled to room temperature. Ice cold water (15 mL) and NH_4PF_6 (15 mg) were then added, resulting in the formation of a yellow precipitate which was filtered, washed with ice cold water (200 mL) and dried under reduced pressure to give **1** as a yellow solid (26 mg, 82%): ^{1}H NMR (400 MHz, $(CD_3)_2CO$) δ 9.25 (d, 1H, J = 4.4 Hz), 8.90 (d, 2H, J = 4.4 Hz), 7.95 (t, 2H, J = 7.2 Hz), 7.64 (t, 1H, J = 7.2 Hz), 7.49 (d, 2H, J = 7.6 Hz), 7.40 (t, 2H, J = 7.2 Hz), 7.33 (t, 1H, J = 7.2 Hz), 7.12 (d, 1H, J = 7.6 Hz), 5.53 (t, 2H, J = 7.2 Hz), 4.65 (s, 2H), 2.93 (s, 3H), 2.57 (s, 3H), 2.68–2.42 (m, 6H); IR (KBr) ν_{max} (cm^{-1}) 3247, 3116, 2943, 2874, 2360, 2342, 2271, 1701, 1608, 1570, 1486, 1443, 1426, 1365, 1317, 1287, 1250, 1211, 1160, 1114, 1084, 1053, 1036, 991, 932, 838, 764, 751, 740, 715, 668; UV–vis (DMSO) λ_{max} = 390 nm (ε = 9200 M^{-1} cm^{-1}); ESMS calculated for $C_{25}H_{28}F_6N_6PRu$ ($[M - PF_6^-]^+$): 659.1068, found ($[M - PF_6^-]^+$): 659.0580; Anal. Calcd for $C_{26.3}H_{32}F_{12}N_6P_2O_{0.6}Ru$ (**1**·0.3Et_2O·0.3H_2O): C, 37.91; H, 3.87; N, 10.07, found: C, 37.91; H, 3.74; N, 10.21.

[Ru(1-isocyTPQA)(CH$_3$CN)$_2$](PF$_6$)$_2$ (*2*)—To a solution of 1-isocyTPQA (15 mg, 0.040 mmol) in 4.6 mL of dry MeOH under inert atmosphere in a pressure flask, *cis*-$[Ru(DMSO)_4Cl_2]$ (19 mg, 0.040 mmol) was added. The solution was then purged with Ar for 10 min at room temperature, and the reaction mixture was allowed to reflux for 5 h under inert atmosphere, during which time the color of the reaction mixture changed from pale yellow to dark red. The reaction mixture was cooled to room temperature and concentrated under reduced pressure. To the flask, a mixture of CH_3CN:H_2O (1:1 v/v, 4.6 mL) was added, and the reaction mixture was refluxed for another 16 h under inert atmosphere. The reaction mixture was again cooled to room temperature. Ice cold water (15 mL) and NH_4PF_6 (15 mg) were then added, resulting in the formation of a yellow precipitate which was filtered, washed with ice cold water (200 mL) and dried under reduced pressure to give **2** as a yellow solid (16 mg, 47%): ^{1}H NMR (400 MHz, $(CD_3)_2CO$) δ 9.12 (d, 1H, J = 6.4 Hz), 8.97 (d, 2H, J = 5.2 Hz), 8.03 (d, 1H, J = 8.4 Hz), 7.94–7.86 (m, 3H), 7.81 (d, 1H, J = 6.4 Hz), 7.74 (t, 1H, J = 7.6 Hz), 7.60 (t, 1H, J = 7.6 Hz), 7.50 (d, 2H, J = 8.0 Hz), 7.36 (t, 2H, J = 6.8 Hz), 5.63 (d, 2H, J = 10 Hz), 5.24 (d, 2H, J = 6.4 Hz), 2.98 (s, 3H), 2.60 (s, 3H), 2.56–2.53 (m, 4H), 2.50–2.44 (m, 2H); IR (KBr) ν_{max} (cm^{-1}) 3422, 2950, 2876, 2276, 1701, 1606, 1563, 1508, 1467, 1421, 1405, 1362, 1319, 1251, 1221, 1160, 1117, 1083, 1050, 992, 966, 840, 768, 758, 740; UV–vis (DMSO) λ_{max} = 390 nm (ε = 11 900 M^{-1} cm^{-1}); ESMS calculated for $C_{29}H_{30}F_6N_6PRu$ ($[M - PF_6^-]^+$): 709.1225, found ($[M - PF_6^-]^+$): 709.1170; Anal. Calcd

for $C_{30.5}H_{33}F_{12}N_6O_{0.5}P_2Ru$ (**2**·0.5$(CH_3)_2CO$): C, 41.50; H, 3.77; N, 9.52, found: C, 41.17; H, 3.78; N, 9.73.

[Ru(cyTPA)(py)$_2$](PF$_6$)$_2$ (*3*)—To a solution of cyTPA (20 mg, 0.061 mmol) in 6.0 mL of dry MeOH under inert atmosphere in a pressure flask, *cis*-[Ru(DMSO)$_4$Cl$_2$] (29 mg, 0.061 mmol) was added. The solution was then purged with Ar for 10 min at room temperature, and the reaction mixture was allowed to reflux for 5 h under inert atmosphere, during which time the color of the reaction mixture darkened slightly. The reaction mixture was cooled to room temperature and concentrated under reduced pressure. To the flask, a mixture of pyridine:H_2O (1:1 v/v, 6.0 mL) was added, and the reaction mixture was refluxed for another 16 h under inert atmosphere. The reaction mixture was then cooled to room temperature. Ice cold water (15 mL) and NH_4PF_6 (15 mg) were added to the reaction mixture, resulting in the formation of an orange precipitate which was filtered, washed with ice cold water (200 mL) and dried under reduced pressure to give **3** as an orange solid (45 mg, 84%): ^{1}H NMR (400 MHz, $(CD_3)_2CO$) δ 8.98 (d, 2H, J = 4.8 Hz), 8.85 (d, 2H, J = 5.2 Hz), 8.76 (d, 1H, J = 5.6 Hz), 8.33 (d, 2H, J = 6.0 Hz), 8.14 (t, 1H, J = 7.6 Hz), 8.00 (t, 2H, J = 7.6 Hz), 7.95 (t, 1H, J = 7.6 Hz), 7.70 (t, 2H, J = 7.2 Hz), 7.62 (t, 1H, J = 7.6 Hz), 7.57 (d, 2H, J = 8.0 Hz), 7.48 (t, 2H, J = 6.4 Hz), 7.39 (t, 2H, J = 7.2 Hz), 7.26–7.22 (m, 2H), 5.17 (dd, 2H, J = 11.2 Hz), 4.71 (s, 2H), 2.61–2.41 (m, 6H); IR (KBr) ν_{max} (cm^{-1}) 3441, 2963, 2350, 1777, 1708, 1605, 1485, 1466, 1445, 1321, 1297, 1217, 1162, 1117, 1066, 993, 838, 770, 759, 711, 701; UV–vis (DMSO) λ_{max} = 360 nm (ε = 12 800 M^{-1} cm^{-1}), 410 nm (ε = 9140 M^{-1} cm^{-1}); ESMS calculated for $C_{31}H_{32}F_6N_6PRu$ ([M – PF$_6^-$]$^+$): 735.1382, found ([M – PF$_6^-$]$^+$): 735.1263; Anal. Calcd for $C_{31}H_{32}F_{12}N_6P_2Ru$: C, 42.33; H, 3.67; N, 9.55, found: C, 42.25; H, 3.71; N, 9.48.

[Ru(1-isocyTPQA)(py)$_2$](PF$_6$)$_2$ (*4*)—To a solution of 1-isocyTPQA (15 mg, 0.039 mmol) in 4.5 mL of dry MeOH under inert atmosphere in a pressure flask, *cis*-[Ru(DMSO)$_4$Cl$_2$] (19 mg, 0.039 mmol) was added. The solution was then purged with Ar for 10 min at room temperature, and the reaction mixture was allowed to reflux for 5 h under inert atmosphere, during which time the color of the reaction mixture changed from pale yellow to dark red. The reaction mixture was cooled to room temperature and NH_4PF_6 (15 mg) was then added, resulting in the formation of a yellow precipitate which was filtered and washed with ice cold water (200 mL). The solid was collected, distilled water (6.0 mL) and 3 to 4 drops of trifluoromethanesulfonic acid were added, and the reaction mixture was refluxed for another 4 h under inert atmosphere. During this time, the color of the reaction mixture changed from dark red to green. The reaction mixture was cooled to room temperature, and ice cold water (15 mL) and NH_4PF_6 (15 mg) were then added, resulting in the precipitation of green [Ru(1-isocyTPQA)(H_2O)$_2$](PF$_6$)$_2$. The green solid was filtered, washed with ice cold water (200 mL) and dried under reduced pressure. It was then treated with pyridine (31 mg, 0.39 mmol) in 6.0 mL of absolute EtOH under inert atmosphere in a pressure flask. The solution was purged with argon for 10 min at room temperature. The mixture was then allowed to reflux for another 16 h under inert atmosphere, and the color of the reaction mixture was observed to change from green to dark red. The reaction mixture was again cooled to room temperature and concentrated under reduced pressure, washed with toluene (20 mL), and extracted with dichloromethane and water. The organic layer was

collected, dried over Na_2SO_4, and concentrated under reduced pressure to give the crude product. The crude product was purified by chromatography on alumina using acetone/hexane (8:2, v/v) as the eluent to give **4** as a red solid (14 mg, 38%): ^{1}H NMR (400 MHz, $(CD_3)_2CO$) δ 9.06 (d, 2H, J = 5.2 Hz), 8.93 (d, 2H, J = 5.6 Hz), 8.60 (d, 1H, J = 6.8 Hz), 8.38 (d, 2H, J = 5.2 Hz), 8.18–8.14 (m, 2H), 7.98–7.90 (m, 4H), 7.77–7.71 (m, 4H), 7.63 (t, 1H, J = 7.6 Hz), 7.57 (d, 2H, J = 8.0 Hz), 7.46–7.39 (m, 4H), 5.31–5.25 (m, 4H); IR (KBr) ν_{max} (cm^{-1}) 3437, 2959, 1607, 1566, 1508, 1487, 1465, 1445, 1404, 1276, 1161, 1085, 839, 759, 740, 704; UV–vis (DMSO) λ_{max} = 360 nm (ε = 10 600 M^{-1} cm^{-1}), 415 nm (8020 M^{-1} cm^{-1}); ESMS calculated for $C_{35}H_{34}F_6N_6PRu$ ($[M - PF_6^-]^+$): 785.1540, found ($[M - PF_6^-]^+$): 785.1445; Anal. Calcd for $C_{39}H_{44}F_{12}N_6OP_2Ru$ (**4**·Et_2O): C, 46.66; H, 4.42; N, 8.37, found: C, 46.37; H, 4.27; N, 8.25.

Methods and Instrumentation

^{1}H and ^{13}C NMR spectra were recorded on either a Varian FT-NMR Agilent 400 MHz, Oxford 500 MHz, or Agilent DD2 600 MHz spectrometer in $CDCl_3$, CD_3OD or $(CD_3)_2CO$, and the spectra were referenced to the residual protonated solvent peaks. Mass spectra were recorded on a time-of-flight Micromass LCT Premier XE Spectrometer, IR spectroscopy was conducted on a Nicolet FT-IR spectrophotometer (KBr pellet), and electronic absorption spectra were recorded on a Varian Cary 50 or an Agilent 8454 spectrophotometer.

Single crystal X-ray diffraction data were collected at 100 K with Mo Kα radiation using a Bruker X8 diffractometer equipped with a kappa geometry goniometer, graphite monochromator, and an APEX-II CCD. The frames were integrated with the Bruker SAINT software package[62] using a narrow-frame algorithm, and the data were corrected for absorption effects using the multiscan method (SADABS).[63] Using Olex2,[64] structures of **1** and **2** were solved with the SHELXS-1997 structure solution program[65] using direct methods and refined with the SHELXL refinement package[66] using least-squares minimization. The structure of **3** was solved with the SHELXT structure solution program[67] using direct methods and refined as with **1** and **2**. During the refinement of structure **1**, a disordered PF_6^- counterion was removed and modeled using a solvent mask. All non-hydrogen atoms were refined anisotropically, and hydrogen atoms were placed in calculated positions. Crystals of **1** were yellow. 200 837 reflections were collected and merged into 12 344 independent reflections with R_{int} = 0.0334. The asymmetric unit contains one Ru complex and 1.5 PF_6^- counterions. The phosphorus atom of one of the PF_6^- ions sits on a special position and is 1/2 occupied, which may be due to an invisible counterion (like H^+) in the electron density map. Crystals of **2** were also yellow. 23 2068 reflections were collected and merged into 21 952 independent reflections with R_{int} = 0.0273. The asymmetric unit contains one Ru complex, two PF_6^- counterions and one CH_3CN in the solvent area. Crystals of **3** were again yellow, and 91 822 reflections were collected and merged into 6547 independent reflections with R_{int} = 0.0837. The asymmetric unit contains one Ru complex and two PF_6^- counterions. Any counterions or solvent molecules present were not shown in the ORTEP diagrams for clarity.

The irradiation source for photolysis and ligand exchange quantum yield experiments was a 150 W Xe arc lamp (USHIO) in a MilliArc lamp housing unit powered by a LPS-220 power

supply equipped with a LPS-221 igniter (PTI). A 395 nm long-pass filter (CVI Melles Griot) was used for the photolysis experiments, while a 400 nm bandpass filter (Thorlabs) with a 335 nm long-pass filter (CVI Melles Griot) was used to measure quantum yields of ligand exchange. For both the photolysis and ligand exchange quantum yield experiments, the samples were dissolved in H_2O with <5% acetone added for solubility. Potassium tris(ferrioxalate) was used as a chemical actinometer to determine the photon flux of the lamp at 400 nm as previously described (1.6×10^{-7} mol photons/min).[68] For NMR studies, solutions of **1** and **2** in CD_3CN (~2 mM) were prepared and stored for 1 h in the dark, and then were irradiated in an NMR tube using the 150 W Xe arc lamp and a 395 nm long-pass filter. ^{1}H NMR spectra were collected using a Bruker DPX 400 MHz spectrometer at the indicated time intervals, and all chemicals shifts were referenced to the residual protonated solvent peak (δ = 1.94 ppm).

Spin restricted and unrestricted density functional theory (DFT) calculations were performed with the Gaussian 09 package.[69] All geometry optimization and vibrational frequency calculations were performed with the SDD[70] basis set on Ru and the TZVP[71] basis set on all other atoms with the PBE[72,73] exchange-correlation functional. The geometries of all complexes were fully optimized starting from X-ray crystal structures, when available. All optimized geometries have positive harmonic frequencies, confirming the calculated structures as electronic energy minima. Further calculations of molecular orbitals and time-dependent DFT (TD-DFT) utilized the B3LYP[74–76] hybrid functional, again with the SDD basis set on Ru and with the TZVP basis set on all other atoms with the inclusion of solvation effects using the polarized continuum model (PCM) with acetonitrile as the solvent in the TD calculations.[77] TD-DFT was used to calculate the electronic transition state energies and intensities of the 75 lowest-energy states. Spin densities were calculated using Mulliken population analysis methods (MPA). Orbitals from the Gaussian calculations were plotted using the Chemcraft program. The analysis of the MO compositions in terms of fragment orbitals, Mayer bond orders, and charge decomposition analyses[78,79] (CDA) were performed using AOMix-FO[80] within the AOMix program.[80,81] CDA and its applications have been previously described in detail by Gorelsky and co-workers.[82,83]

Ultrafast transient absorption data were collected on a broadband UV–vis system (Figure S23, Supporting Information) consisting of a Ti:sapphire oscillator (Vitara-S, Coherent), which generated 20 fs pulses at 80 MHz to seed a high-energy Ti:sapphire regenerative amplifier (Astrella 1K-USP, Coherent) to produce 7 mJ, 35 fs pulses at 1 kHz. The output from the regenerative amplifier was then split, where 1 mJ was used to generate a white light continuum as previously described,[84] and the remaining 6 mJ was split again using a 50:50 beamsplitter. From the latter, 3 mJ was used to pump an OPA (OPerA Solo, Coherent/Positive Light) to generate a pump pulse tunable from 300–2500 nm. A thermoelectrically cooled CCD camera (Princeton Instruments, 1340×100 pixels) and home-developed software, written in LabVIEW 2015, were used to collect the spectral data. An instrument response full width at half-maximum (fwhm) of ~85 fs was measured using the optical Kerr effect in cyclohexane. Typically, a total sample volume of ~10–20 mL was circulated through a Harrick Scientific flow cell (1 mm thick CaF_2 windows, 1 mm optical path length). The sample solutions were prepared with an absorbance at the excitation wavelength

of ~0.5–0.6, and the pump pulse energy was set to ~2 μJ at the sample. All other aspects of the optical setup and data collection are as previously described.[84] The samples were excited with 350 nm, and the polarization angle between the pump and probe beams was set to the magic angle of 54.7° to avoid effects caused by rotational diffusion. Measurements were repeated three times at each time delay by collecting three retroreflector cycles and the spectra were corrected for the chirp in the white light continuum.[85] The kinetic traces were fit to mono- or biexponential decays as needed.[86]

RESULTS AND DISCUSSION

Synthesis and X-ray Crystallography

The precursor (2*R*,6*S*)-2,6-di(pyridin-2-yl)piperidine (structure shown in Figure 1) was synthesized according to a known literature procedure[60] in which the commercially available starting material 2-pyridinecarboxaldehyde was treated with 1,3-acetonedicarboxylic acid in the presence of ammonium acetate, followed by a Wolff–Kishner reaction. The ligand cyTPA was prepared by treating (2*R*,6*S*)-2,6-di(pyridin-2-yl)piperidine with 2-picolyl chloride hydrochloride, NaI·2H_2O and DIPEA in CH_3CN at 50 °C through alkylation. The ligand 1-isocyTPQA was synthesized following a similar procedure using 1-(chloromethyl)isoquinoline (Figure 1).

Treating each ligand with 1 equiv of *cis*-[Ru(DMSO)$_4$Cl$_2$] in MeOH at 70 °C provided a 2:1 mixture of [Ru(L)(DMSO)-Cl]Cl stereoisomers (L = cyTPA, 1-isocyTPQA) as previously described in the literature.[87] Heating [Ru(L)(DMSO)Cl]Cl in a CH_3CN:H_2O mixture (1:1, v/v) resulted in the formation of the corresponding [Ru(cyTPA)$(CH_3CN)_2]^{2+}$ (**1**) and [Ru(1-isocyTPQA)$(CH_3CN)_2]^{2+}$ (**2**) complexes in good yield. Heating [Ru(cyTPA)(DMSO)Cl]Cl at 80 °C under similar conditions in the presence of 10 equiv of pyridine, followed by precipitation with NH_4PF_6 resulted in [Ru(cyTPA)$(py)_2$]-$(PF_6)_2$ (**3**) in 84% yield. The precipitation of [Ru(1-isocyTPQA)(DMSO)Cl]Cl with NH_4PF_6, followed by heating in distilled H_2O with trifluoromethanesulfonic acid at 100 °C afforded the intermediate complex [Ru(1-isocyTPQA)-$(H_2O)_2$]$(PF_6)_2$ as a green solid. Treating [Ru(1-isocyTPQA)-$(H_2O)_2$]$(PF_6)_2$ with 10 equiv of pyridine in absolute EtOH at 80°C resulted in [Ru(1-isocyTPQA)$(py)_2$]$(PF_6)_2$ (**4**) in moderate yield.

Diffusion of diethyl ether into solutions of **1–3** in acetone provided single crystals suitable for X-ray crystallographic analysis (Figure 2). Additional crystallographic data for **1–3**, including data collection parameters, are detailed in Tables S1–S3 (Supporting Information), with selected bond lengths and bond angles listed in Tables S2 and S3. For all three structures, the N6 donor is defined as that which is positioned *cis* to the basic nitrogen N3, while the N1 atom is positioned *trans* to N3 (Figure 2).

Complex **1** crystallizes in the monoclinic space group $C2/c$ with $Z = 4$. The coordination environment around the Ru(II) metal center exhibits a slightly distorted octahedral geometry, with bond angles ranging from 79.36(7)° to 101.15(7)°. In **1**, the fourth arm of the tetradentate cyTPA ligand (the N5 arm) is slightly tilted toward the N2 arm, causing the N5–Ru1–N2 angle to be 84.95(7)°, a value smaller than the analogous angle in [Ru(TPA)$(CH_3CN)_2]^{2+}$, 90.4(2)°.[56] Furthermore, the rigidity afforded by the piperidine ring in **1**

appears to cause a small amount of additional steric strain in the cyTPA ligand as evidenced by the slightly smaller N2–Ru1–N4 angle of 159.15(7)° as compared to 164.1(2)° in $[Ru(TPA)\text{-}(CH_3CN)_2]^{2+}$.[56] These small distortions do not cause a significant lengthening of any of the Ru–N bonds in **1**, since the bond distances are all within a few hundredths of an Ångstrom to those reported for $[Ru(TPA)(CH_3CN)_2]^{2+}$,[56] and the Ru–N(CH_3CN) bond lengths in **1** are comparable to those reported for *cis*-$[Ru(bpy)_2(CH_3CN)_2]^{2+}$.[88]

Complex **2** crystallizes in the monoclinic space group $P2_1/n$ with $Z = 4$. The coordination environment around the metal center also exhibits a slightly distorted octahedral geometry, with bond angles ranging from 80.98(3)° to 99.80(4)°. As expected, the substitution of a pyridine for an isoquinoline moiety in the N5 arm of the tetradentate ligand does not produce steric strain around the metal center. A comparison between the bond angles of **1** and **2** reveals that the only difference is that in **2** the N6 CH_3CN *cis* to the basic amine nitrogen is tilted slightly toward the N2 arm, as evidenced by the slightly smaller N6–Ru1–N2 angle of 86.99(3)° in **2** as compared to 93.00(7)° in **1**. Again, the Ru–N bond lengths in **2** are comparable to **1**, as well as to those of the previously reported $[Ru(TQA)(CH_3CN)_2]^{2+}$.[58] In addition, the Ru–N(CH_3CN) bond lengths in **2** also compare well with those reported for *cis*-$[Ru(bpy)_2(CH_3CN)_2]^{2+}$.[88]

Complex **3** crystallizes in the monoclinic space group $P2_1/c$ with $Z = 4$. The coordination environment around the Ru(II) metal center again exhibits a slightly distorted octahedral geometry with bond angles ranging from 76.8(4)° to 101.9(4)°. In **3**, the N5 arm of the cyTPA ligand is bent toward the N4 arm to a larger degree than that in **1** or **2**, as evidenced by the smaller N5–Ru1–N4 angle of 80.7(5)° in **3**. This difference is attributed to the steric bulk afforded by a py ligand as compared to an CH_3CN in **1** and **2**. The N2 and N4 arms of the cyTPA ligand cause the N1 py ligand to be canted rather than coplanar, as is the case in **1** and **2** with CH_3CN ligands, which pushes the N5 arm of cyTPA closer to the N4 arm, as well as the N2 arm closer to the central piperidine ring. This steric clashing between the N1 py and the tetradentate ligand is also observed in $[Ru(TPA)(py)_2]^{2+}$.[57] The Ru–N bond lengths of the tetradentate ligand in **3** are similar to the corresponding bond lengths in **1** and **2**, and the Ru–N(py) bond lengths of **3** are similar to those measured in $[Ru(TPA)(py)_2]^{2+}$,[57] as well as in *cis*-$[Ru(bpy)_2(py)_2]^{2+}$.[89]

Electronic Absorption Spectroscopy and Photochemistry

The electronic absorption spectra of the CH_3CN complexes **1** and **2** are displayed in Figure 3 and exhibit ^{1}MLCT-based absorption features with maxima at 390 nm (ε = 9200 M^{-1} cm^{-1} and 11 900 M^{-1} cm^{-1}, respectively). Ligand-centered $^3\pi\pi^*$ transitions of the ligands in **1** and **2** result in strong absorption in the ultraviolet range. The intensities of these transitions correlate well with those of $[Ru(TPA)\text{-}(CH_3CN)_2]^{2+}$; however, the ^{1}MLCT absorption of **2** is red-shifted as compared to those of **1** and $[Ru(TPA)\text{-}(CH_3CN)_2]^{2+}$,[56] attributed to the presence of the quinoline moiety in the tetradentate ligand (Figure 3). The pyridine complexes **3** and **4** exhibit ^{1}MLCT transitions at 360 nm (ε = 12 800 M^{-1} cm^{-1} and 10 600 M^{-1} cm^{-1}, respectively). Shoulders of this peak in **3** and **4** are observed at ~410 nm ($\varepsilon \sim$ 9140 M^{-1} cm^{-1}) and ~415 nm ($\varepsilon \sim$ 8020 M^{-1} cm^{-1}), respectively, that tail to ~500 nm (Figure S24, Supporting Information). The ^{1}MLCT absorption maxima of **3** and **4** are red-

shifted compared to the analogous CH_3CN complexes, as is well-known for other *cis*-Ru(II) complexes coordinated by two CH_3CN and py ligands.[37,90] The quinoline moiety in **4** leads to a further red shift as compared to **3**. Again, the intensities of these transitions are in good agreement with those of $[Ru(TPA)(py)_2]^{2+}$.[57]

The irradiation of **1–4** in H_2O (<5% acetone) results in changes to the absorption spectra of each complex ($\lambda_{irr} \geq 395$ nm), whereas no changes are observed under similar conditions when the solutions of each complex are kept in the dark for at least 6 h (Figure S25, Supporting Information). The spectral changes observed for **1** and **2** are shown in Figure 4, and those for **3** and **4** appear in Figure S26 (Supporting Information). The photolysis of **1** is complete within 27 min, as no additional spectral changes are observed after this time. In contrast, the conversion of **2** to product is complete within only 9 min under similar experimental conditions. This difference in photo-chemical activity is reflected in the difference in the measured quantum yields, Φ_{400}, for the two complexes (λ_{irr} = 400 nm, Table 1), where **2** is 5-fold more photoactive than **1**. In contrast to the CH_3CN complexes **1** and **2**, those containing py at the N1 and N6 positions, **3** and **4**, require at least 2 h of irradiation to reach completion under similar experimental conditions. The values of Φ_{400} for **3** and **4** are comparable, but both are ~30-fold lower than that measured for **2** (Table 1). The less efficient photochemistry of py Ru(II) complexes as compared to analogous CH_3CN compounds is well documented in the literature.[14,27,48,51]

During the photolysis of **1–4** in H_2O, a decrease in the ^{1}MLCT absorption band of each complex is observed with a concomitant increase in a peak at lower energies, as well as well-defined isosbestic points indicative of the formation of a single product from the reactant. For example, the irradiation of **2** in H_2O results in a decrease of the ^{1}MLCT absorption at 383 nm and a growth of a new absorption peak with maximum at 414 nm, resulting in an isosbestic point at 399 nm. On the basis of prior work on related complexes, it is expected that one of the CH_3CN ligands in **1** and **2** and py in **3** and **4** exchanges with a solvent H_2O molecule upon irradiation.

As discussed above, the ligand exchange quantum yield of **2** is 5-fold greater than that of **1,** and it was shown in previous work that steric hindrance leads to enhanced ligand dissociation.[91] The major structural difference between **1** and **2** is the substitution of the third pyridine in the cyTPA ligand in **1** for a quinoline moiety in the 1-isocyTPQA ligand in **2**. However, the quinoline moiety in **2** is oriented away from the metal center, such that it is not expected to contribute to steric distortions around the metal or to weaken the Ru–N(CH_3CN) bonds. In fact, the ground state bond lengths and angles observed in the X-ray crystal structures are similar between **1** and **2**, inconsistent with a weaker Ru–N bond induced by steric clash. Therefore, it may be concluded that the increased quantum yield in **2** must be associated with differences in electronic structure afforded by the presence of the quinoline arm in **2** as compared to a pyridine arm in **1**.

In order to gain additional structural information on the products formed upon irradiation, the photolyses of **1** and **2** were also followed using ^{1}H NMR spectroscopy in CD_3CN (Figure S27 and Figure 5, respectively). No spectral changes are observed for either complex in the dark in CD_3CN (1 h). However, upon irradiation the resonance at 2.39 ppm in **1** ($\lambda_{irr} \geq$

395 nm, 10 min) associated with the protons of the N6 CH_3CN ligand *cis* to the basic nitrogen and *trans* to the pyridine arm of the cyTPA begins to decrease in intensity. A similar decrease is observed for the signal at 2.41 ppm upon irradiation of **2** ($\lambda_{irr} \geq 395$ nm, 5 min), which corresponds to the bound N6 CH_3CN ligand positioned *cis* to the basic nitrogen and *trans* to the quinoline arm of the 1-isocyTPQA ligand. This behavior is associated with the exchange of the bound CH_3CN ligand for solvent CD_3CN and continues until the process is complete. As expected, in both complexes there is an increase in intensity of the peak corresponding to free CH_3CN, which appears at 1.96 ppm in CD_3CN. Continued irradiation leads to the complete exchange of the N6 CH_3CN ligand in 90 min for complex **1**, a process that is complete in 25 min in **2**. The aromatic regions of the NMR spectra of **1** and **2** remain unchanged throughout the photolysis experiments (Figures S28 and S29, respectively, Supporting Information), indicating that the only reaction is the exchange of CH_3CN for CD_3CN in the complex, thus retaining its electronic and structural characteristics.

CALCULATIONS

Density functional theory (DFT) calculations were utilized to gain a better understanding of the bonding and electronic structure of **1–4**. Geometry optimizations for these complexes in the singlet ground state produced calculated structures in good agreement with crystallographic data (Tables S4–S7, Supporting Information), as well as ν(CN) of the CH_3CN ligands of **1** and **2** that are in good agreement with experimental IR data. The electronic structures of these complexes in the ground state can be described by frontier molecular orbitals that are similar across the series. The HOMOs of **1–4** are mostly composed of Ru d-orbital character with some ligand mixing, featuring 70–81% metal localization in **1**, **3**, and **4** (Figure 6). Interestingly, the HOMO of **2** exhibits the lowest Ru d character, 62%, with the highest ligand mixing of the series. The LUMOs are exclusively either localized on the cyTPA ligand of **1** and **3** or 1-isocyTPQA of **2** and **4**.

Time-dependent DFT, TD-DFT, calculations for **1–4** show remarkable similarities for the four lowest energy transitions of the complexes, all of which involve the ruthenium metal center and the tetradentate ligand (Table S8, Supporting Information). The calculated lowest ^{1}MLCT absorption bands of **1** and **3** exhibit Ru(d_π) → π^*(cyTPA) character with energies of 26 500 cm^{-1} and 24 600 cm^{-1}, respectively, which compare well with the corresponding experimental values of 25 800 cm^{-1} and 24 400 cm^{-1}. Similarly, the lowest ^{1}MLCT Ru(d_π) → π^*(1-isocyTPQA) transitions are calculated for **2** at 25 600 cm^{-1} and **4** at 24 400 cm^{-1}, in good agreement with the experimental maxima at 25 000 cm^{-1} and 24 200 cm^{-1}, respectively. Notably, unlike **1**, **3**, and **4**, one of the low-energy transitions calculated for **2** exhibits some mixing of ligand-centered 1-isocyTPQA $^1\pi\pi^*$ character into the broad ^{1}MLCT band and another is solely attributable to 1-isocyTPQA $^1\pi\pi^*$ (Table S8). This finding is consistent with the larger amount of ligand mixing in the HOMO of **2**, which is absent in **1**, **3**, and **4**, as well as the participation of the ligand-centered HOMO–3 in the low energy transitions of **2**.

Geometry optimizations and vibrational frequency calculations were also completed in the triplet states of **1–4**. It should be noted that the optimized structures for **1**, **3**, and **4** yielded structures in which the Ru–N bonds of the tetradentate cyTPA and 1-isocyTPQA ligands

were severely elongated in the triplet state, possibly suggesting facile dissociation of one of these arms in the excited state (Tables S4–S7). In contrast, these elongations were not observed in the optimized structure of the lowest triplet state of **2** (Table S5). These differences for **2** relative to the other complexes are of interest given its significantly more efficient ligand exchange upon irradiation.

Mulliken spin density calculations were performed to determine the spin density on the Ru(II) center and to examine the nature of the triplet state. For complexes with a ^{3}MLCT as the lowest energy triplet state, the Mulliken spin density on the ruthenium center should theoretically equal 1, indicative of one unpaired electron on the metal. Those complexes with a ^{3}LF as the lowest energy triplet state should have a spin density of about 2 on the ruthenium center, indicating two unpaired electrons on the metal. Any complex with a spin density on the metal that is not close to values of 1 or 2 suggests some level of ligand mixing. For complexes **1**, **3**, and **4**, the Mulliken spin densities on the Ru(II) center were calculated to be 1.63, 1.75, and 1.73, respectively. These spin densities are consistent with a ^{3}LF state as the lowest energy triplet state with some spin localization on the ligands. Surprisingly, for complex **2**, the Mulliken spin density on the metal was calculated to be 0.37, which is extremely low for a ^{3}MLCT state and is more consistent with significant mixing from a ligand-centered state. Figure 7 shows a comparison of the Mulliken spin densities on the atoms of complexes **1** and **2**. Notably, the majority of the spin density in **2** is localized on the quinoline arm of the 1-isocyTPQA ligand, with only minimal contributions from other atoms.

Although **2** exhibits the most efficient photoinduced CH_3CN ligand exchange with solvent, it is surprising that it is the only complex in the series that does not feature a ^{3}LF state as the lowest energy triplet state. It should be noted, however, that the ^{3}LF states of **1**, **3**, and **4** appear to be dissociative taking into account the elongated bonds of the tetradentate ligand. This result indicates that if the ^{3}LF state is accessed in these complexes, then an arm of the tetradentate ligand may be dissociated upon irradiation, which would likely recoordinate without resulting in an overall chemical transformation. Therefore, irradiation of these complexes would not result in the exchange of CH_3CN in **1** or py in **3** and **4**.

^{1}H NMR spectroscopy shows that the CH_3CN ligand that dissociates more readily in **2** is positioned *trans* to the quinoline moiety in the tetradentate ligand. In general, σ-donation from py- and quinoline-type ligands is stronger than that of nitrile-containing ligands. Instead, the CH_3CN ligand relies heavily on π-back-donation for bonding to ruthenium. Charge decomposition analysis (CDA), a theoretical method used to quantify the total electron donation and back-donation between the metal and each ligand, was used to determine these quantities in **1** and **2**. The back-donation from the Ru center to the photolabile N6 CH_3CN ligand in **2** decreases by 23% in the triplet state as compared to the singlet ground state, as the ruthenium center is partially oxidized in the excited state (Table S17, Supporting Information). The corresponding cyTPA complex, **1**, possesses a py moiety rather than quinoline in the tetradentate ligand, and shows a decrease in back-donation to the CH_3CN ligand from the singlet state to the triplet state of less than 10%.

This trend was further examined by analyzing the Mayer bond orders (MBOs) of the Ru–N bonds. MBOs offer insight into the relative covalency vs ionicity of a bond and are an extension of Wiberg bond orders, a classical view of bonding, and can be related to the bond strength.[92] Previous theoretical studies have shown that MBO analysis is a useful tool in describing bonding in transition metal systems.[92–97] For **2**, the MBO analysis shows a dramatic 57% increase in Ru–N(quinoline) bond strength and a 14% decrease in Ru–N(CH_3CN) bond strength in the CH_3CN ligand *trans* to the quinoline moiety (N6 CH_3CN) in the triplet state. The quinoline moiety, therefore, exerts a *trans*-type influence on this CH_3CN ligand, greatly weakening the Ru–N(CH_3CN) bond, promoting dissociation in the triplet excited state. This weakening does not occur in the corresponding py complex, **4**, due to the similar σ–bond strengths between quinoline and the leaving py ligand. In this complex, the MBO of the Ru–N(py) decreases only by ~2% in the triplet state, while the Ru–N(quinoline) MBO increases by 3%. A similar trend is observed for complexes **1** and **3** at the same positions, but with increased MBOs calculated from the ground state to the lowest triplet state for both Ru–N(CH_3CN) and Ru–N(py) bonds, respectively (Table 2). The observation of *trans* influence and *trans* effect in ruthenium complexes has been reported previously, specifically with phosphine and py-type ligands in the ground state.[98–101] To our knowledge, there are no reports of *trans* influence in the excited state that directly results in ligand dissociation. From the results of the Mulliken spin density calculations, in combination with the CDA and MBO analyses, it may be inferred that the high quantum yield of ligand dissociation observed for **2** is associated with the high spin density localized on the quinoline moiety in the mixed ^{3}MLCT/$^3\pi\pi^*$ excited state. This ^{3}MLCT/$^3\pi\pi^*$ state must induce a *trans*-type influence, allowing for efficient ligand dissociation of the N6 CH_3CN ligand.

Time-Resolved Spectroscopy

Ultrafast transient absorption spectroscopy was used to compare the nature of the excited states of **1** and **2**, since the latter undergoes ligand exchange with 5-fold greater efficiency than the former. In addition, the transient absorption spectra of **3** and **4** were also collected and are shown in the Supporting Information. It is well established that intersystem crossing (ISC) from the ^{1}MLCT to the ^{3}MLCT state occurs within 15–40 fs in $[Ru(bpy)_3]^{2+}$, as well as in other Ru(II) polypyridyl and related complexes.[90,102,103] As such, the transient absorption signals observed for **1** and **2** after excitation of the ^{1}MLCT state can be attributed to states in the triplet manifold due to the ~85 fs pulse employed in the present experiments.[104]

The transient absorption spectra of **2** collected in CH_3CN following 350 nm excitation are shown in Figure 8a (fwhm = 85 fs), and consist of a ground state bleach from 390 to 438 nm, with positive absorption from 438 to 600 nm and an isosbestic point at 438 nm. Both the bleach at 400 nm and the positive signal with maximum at 465 nm decay monoexponentially with τ = 42 ps (Table 1). No spectral changes are observed from 200 fs to 1 ps (Figure S34a, Supporting Information). The intensity and position of the positive absorption is consistent with a ^{3}MLCT state, similar to the spectral features of ^{3}MLCT states $_{2+}$ of related Ru(II) complexes, including $[Ru(bpy)_2(CH_3CN)_2]$ in CH_3CN.[90] In addition, the simulated transient absorption spectrum of **2** shown in Figure S35b (Supporting Information), created from the

subtraction of the calculated absorption spectrum of ^{3}MLCT/$^3\pi\pi^*$ state and that of the ground state, agrees fairly well with experiment. The lifetime of **2** in CH_3CN is similar to that reported for $[Ru(bpy)_2(CH_3CN)_2]^{2+}$ in the same solvent, 50 ps.[90] In CH_3CN, the photoinduced ligand exchange of **2** does not result in a product that is different than the starting material, such that any kinetics that may be associated with that process are not observed. These results are consistent with the formation of the ^{3}MLCT/$^3\pi\pi^*$ state of **2** within the laser pulse, and that this state decays to regenerate the ground state with τ = 42 ps in CH_3CN. The short lifetime of the ^{3}MLCT/$^3\pi\pi^*$ state can be attributed to competing ligand dissociation.

When the transient absorption experiment is conducted in acetone under similar conditions (Figure 8b), the irreversible formation of the ligand exchange product, [Ru(1-isocyTPQA)-(CH_3CN)(acetone)]$^{2+}$, is observed at long delay times consistent with the spectral changes measured during steady-state photolysis. At earlier times, 1–17 ps, a broad positive signal is observed in the 450–600 nm range which can be fitted to a monoexponential decay with τ = 36 ps. Although the photoproduct absorbs in the 390–440 nm range, the kinetics of the bleach signal at 400 nm are also monoexponential with τ = 36 ps. It should be noted that there are no spectral changes from 100 fs to 1 ps (Figure S34b, Supporting Information). In addition, a power dependence of the product formed in the ultrafast experiment in acetone is consistent with a one-photon process (Figure S36).

Because of the overlap between the bleach signal and that of the product in Figure 8b, the kinetics of product formation could not be measured independently. There are two possibilities for the observation of the same monoexponential time constant for the bleach signal at 390 nm that overlaps with the product absorption and the positive ^{3}MLCT signal at 500 nm, namely that the product is formed directly from the ^{3}MLCT state or that it is generated within the laser pulse and its signal does not change throughout the experiment. In the latter scenario, the ligand exchange dynamics do not contribute to the transient absorption signal in the 1 ps –2.68 ns range, such that the signal of the last trace of Figure 8b collected at 2.68 ns would have been present at all time delays. In the case where the product is formed from the ^{3}MLCT state, the signal in Figure 8b collected at early times would have little contribution from product, and the absorption of the latter would increase exponentially with the measured time constant of 36 ps. A series of additions of product signal collected at 2.68 ns in Figure 8b to the signal from the pure ^{3}MLCT (Figure 8a) were undertaken as described in detail in the Supporting Information and shown in Figure S37. Two exemplary time points at early and late times in the decay, 8 ps (Figure S37c) and 51 ps (Figure S37d), respectively, are used to compare the simulated signals which are consistent with the formation of the photoproduct from the ^{3}MLCT state and not within the laser pulse.

The transient absorption spectra collected for **1** in CH_3CN are similar to those of **2** in the same solvent and are shown in Figure S38 (Supporting Information, λ_{exc} = 350 nm, fwhm = 85 fs). The dominant features are the ground state bleach at ~390 nm and a broad positive transient absorption signal in the 430–600 nm range with maximum at ~460 nm. Both features decay monoexponentially with τ = 36 ps to regenerate the ground state (Table 1). Similar absorption and bleach signals were observed for **1** in acetone with τ = 34 ps. The low quantum yield for ligand exchange in this complex precludes the observation of

different kinetics in CH_3CN and acetone in **1**. Although the lowest energy triplet state of **1** was calculated to be ^{3}LF in nature, from the intensity of the observed excited state absorption, together with spectral and kinetic similarities to **2** and other Ru(II) polypyridyl complexes, it may be concluded that the state observed with 34–36 ps lifetime is the ^{3}MLCT, not the ^{3}LF. In addition, it is evident that the calculated transient absorption spectrum of the ^{3}LF state shown in Figure S39 (Supporting Information) features ~10-fold lower intensity of the positive signal as compared to that calculated for **2**, inconsistent with the experimental data.

The transient absorption spectra of **3** and **4** are shown in Figure S40 (Supporting Information) and exhibit similar features that are red-shifted compared to those of **1** and **2**, respectively. Complex **3** exhibits a ground state bleach at 420 nm and a weak positive transient absorption signal from 470 to 600 nm with τ = 160 ps (Table 1). The identical, monoexponential kinetics of the positive signal and the bleach measured for **3** are indicative of the population of a single state within the laser pulse that returns to the ground state. Similarly, the spectral features of **4** are red-shifted relative to those of the corresponding CH_3CN complex, **2**, and features a ground state bleach at 420 nm and a positive transient absorption signal at >480 nm (Figure S40). These signals decay monoexponentially with τ = 120 ps (Table 1). The ^{3}LF state was calculated as the lowest energy triplet state in both **3** and **4**, with simulated transient absorption spectra for these complexes shown in Figures S41 and S42, respectively (Supporting Information). As is the case with **1**, the positive signal observed for **3** and **4** is significantly stronger than expected for a metal-centered state and can be assigned as ^{3}MLCT states. The broad spectral profiles throughout the visible range are similar to those previously reported for the ^{3}MLCT excited states of the related complexes $[Ru(bpy)_2(py)_2]^{2+}$ and $[Ru(bpy)_2(NA)_2]^{2+}$ (NA = nicotinamide), respectively.[105–107]

Excited State Populations and Ligand Exchange

Although the minimized ^{3}LF state lies at a lower energy than the ^{3}MLCT state in **1**, the latter is observed in the time-resolved absorption spectrum. A possible explanation for this behavior is that ISC from the ^{1}MLCT populates the ^{3}MLCT state in <100 fs, as is typically observed in related Ru(II) polypyridyl complexes.[102,103] Displacement of the ^{3}LF potential energy surface along a given nuclear coordinate, such as elongation of one or more Ru–N bonds in the triplet state, would require that the system overcome an activation barrier to reach the ^{3}LF state (Figure 9). Inspection of Tables S4–S7 reveal that indeed two of the Ru–N bonds to the tetradentate ligand, Ru–N3 and Ru–N4 in **1**, and Ru–N2 and Ru–N4 in **3** and **4**, are significantly elongated in the ^{3}LF state as compared to the ground state. It is evident from Table S4 that the Ru–N3 and Ru–N4 bonds in **1** are elongated by 0.27 and 0.34 Å, respectively, whereas one of the Ru–N(CH_3CN) bonds lengthens by 0.05 Å and the other contracts by 0.01 Å.

For comparison, the calculated bond changes in the ^{3}MLCT/$^3\pi\pi^*$ state of **2** show a small contraction of three of the four Ru–N bonds to the 1-isocyTPQA ligand of <0.035 Å, while the Ru–N2 bond lengthens by only 0.015 Å. Therefore, significant structural changes are expected from the ground and ^{3}MLCT states of **1** to the ^{3}LF state, resulting in a high

activation barrier to populate the ^{3}LF state. The observation of the ^{3}MLCT instead of the lowest energy ^{3}LF states in the transient absorption of **1**, explained by a high activation barrier to populate the ^{3}LF state from the vibrationally cooled ^{3}MLCT state, is consistent with the low quantum yield for ligand exchange in this complex and a lifetime that is similar to that of **2** and related complexes. Similar arguments can be made for complexes **3** and **4**, which exhibit elongation of two of the RuN bonds to the tetradentate ligand of ≥0.3 Å.

CONCLUSIONS

A series of Ru(II) polypyridyl complexes containing two different tetradentate-based frameworks were synthesized and their effectiveness for use as photocages to deliver nitrile or pyridine ligands upon irradiation was explored. The quantum yield for the CH_3CN/H_2O ligand exchange of **2** was measured to be $\mathbf{\Phi}_{400}$ = 0.033(3), 5-fold greater than that of **1**, $\mathbf{\Phi}_{400}$ = 0.0066(3), although this effect cannot be attributed to steric crowding in the former. DFT and related calculations show the presence of a highly mixed ^{3}MLCT/$^3\boldsymbol{\pi\pi}^*$ excited state as the lowest triplet state in **2**, whereas the lowest energy triplet state in **1**, **3**, and **4** was calculated to be ^{3}LF in nature. The mixed ^{3}MLCT/$^3\boldsymbol{\pi\pi}^*$ excited state places significant spin density on the quinoline moiety of the 1-isocyTPQA ligand that is *trans* to the photolabile N6 CH_3CN ligand in **2**. Additionally, MBO analysis reveals that in the triplet state of **2**, the Ru–N(quinoline) bond strength increases while the Ru–N-(CH_3CN) bond strength of the photolabile N6 CH_3CN ligand decreases compared to the singlet ground state, suggesting the presence of a *trans*-type influence in the excited state that leads to the higher value of $\mathbf{\Phi}_{400}$ measured in **2**. The result that complexes with ^{3}LF lowest energy excited states were less photolabile than that with ^{3}MLCT/$^3\boldsymbol{\pi\pi}^*$ lowest energy excited state is counter to the general understanding of Ru(II) photochemistry. Ultrafast spectroscopy was used to probe the excited states of **1–4**, which reveal that the ^{3}LF states are not populated in **1**, **3**, and **4**, consistent with the low yields of ligand exchange product upon irradiation in these complexes. This unusual result is explained by the large elongation of two RuN bonds of the tetradentate ligands in these complexes, thus increasing the activation energy from the ^{3}MLCT to the ^{3}LF states in **1**, **3**, and **4**.

Mixed ^{3}MLCT/$^3\boldsymbol{\pi\pi}^*$ excited states that promote ligand dissociation, such as that of **2**, represent a new manner to effect photoinduced ligand exchange. In addition, ^{3}MLCT deactivation through the lower-lying ^{3}LF state was shown to be avoided through significant structural changes around the metal center in the latter. Both concepts can be used to design improved complexes for applications that require efficient ligand dissociation, such as drug delivery, as well as for those that require minimal deactivation of the ^{3}MLCT state through low-lying metal-centered states. As such, these findings are expected to be useful to fields from photochemotherapy to solar energy conversion and sensing.

Supplementary Material

Refer to Web version on PubMed Central for supplementary material.

Acknowledgments

The authors thank the National Institutes of Health (EB 016072) for their generous support, the Center for Chemical and Biophysical Dynamics (CCBD) at OSU, and the Ohio Supercomputer Center. C.T. acknowledges the partial support from the National Science Foundation (CHE-1465067).

References

1. Balzani V, Bergamini G, Ceroni P. Coord Chem Rev. 2008; 252:2456.
2. Balzani V, Moggi L. Coord Chem Rev. 1990; 97:313.
3. Bonnet S, Collin JP. Chem Soc Rev. 2008; 37:1207. [PubMed: 18497933]
4. Bruijnincx, PCA., Sadler, PJ. Controlling Platinum, Ruthenium, and Osmium Reactivity for Anticancer Drug Design. In: van Eldik, R., Hubbard, CD., editors. Adv Inorg Chem. Vol. 61. Academic Press; Burlington, MA: 2009. p. 1-62.
5. Ceroni P, Credi A, Venturi M. Chem Soc Rev. 2014; 43:4068. [PubMed: 24590055]
6. Grätzel M. Inorg Chem. 2005; 44:6841. [PubMed: 16180840]
7. Kalyanasundaram K, Graetzel M. Curr Opin Biotechnol. 2010; 21:298. [PubMed: 20439158]
8. Kalyanasundaram K. Coord Chem Rev. 1982; 46:159.
9. Smith NA, Sadler PJ. Philos Trans R Soc, A. 2013; 371:20120519.
10. Romanova J, Sadik Y, Ranga Prabhath MR, Carey JD, Jarowski PD. J Phys Chem C. 2017; 121:2333.
11. Pan J, Jiang L, Chan CF, Tsoi TH, Shiu KK, Kwong DWJ, Wong WT, Wong WK, Wong KL. J Lumin. 2017; 184:89.
12. Zigler DF, Morseth ZA, White TA, Canterbury TR, Sayre HJ, Rodríguez-Corrales JÁ, Brennaman MK, Brewer KJ, Papanikolas JM. Inorg Chim Acta. 2017; 454:266.
13. O'Donnell RM, Sampaio RN, Li G, Johansson PG, Ward CL, Meyer GJ. J Am Chem Soc. 2016; 138:3891. [PubMed: 26901780]
14. Knoll JD, Albani BA, Turro C. Acc Chem Res. 2015; 48:2280. [PubMed: 26186416]
15. Ghosh R, Palit DK. Phys Chem Chem Phys. 2014; 16:219. [PubMed: 24247908]
16. Horvath R, Lombard J, Leprêtre JC, Collomb MN, Deronzier A, Chauvin J, Gordon KC. Dalt Trans. 2013; 42:16527.
17. Serpone N, Pelizzetti E, Gratzel M. Coord Chem Rev. 1985; 64:225.
18. Thompson DW, Ito A, Meyer TJ. Pure Appl Chem. 2013; 85:1257.
19. Zhang Y, Galoppini E, Johansson PG, Meyer GJ. Pure Appl Chem. 2011; 83:861.
20. Kärkäs MD, Johnston EV, Verho O, Åkermark B. Acc Chem Res. 2014; 47:100. [PubMed: 23957573]
21. Hammarström L. Acc Chem Res. 2015; 48:840. [PubMed: 25675365]
22. Hartings MR, Kurnikov IV, Dunn AR, Winkler JR, Gray HB, Ratner MA. Coord Chem Rev. 2010; 254:248. [PubMed: 20161508]
23. Anderson BL, Maher AG, Nava M, Lopez N, Cummins CC, Nocera DG. J Phys Chem B. 2015; 119:7422. [PubMed: 25635708]
24. Lo KKW, Li SPY. RSC Adv. 2014; 4:10560.
25. King AW, McClure BA, Jin Y, Rack JJ. J Phys Chem A. 2014; 118:10425. [PubMed: 25137451]
26. Weidmann AG, Komor AC, Barton JK. Comments Inorg Chem. 2014; 34:114.
27. Knoll JD, Turro C. Coord Chem Rev. 2015; 282–283:110.
28. Joshi T, Gasser G. Synlett. 2015; 26:275.
29. Barragán F, López-Senín P, Salassa L, Betanzos-Lara S, Habtemariam A, Moreno V, Sadler PJ, Marchán V. J Am Chem Soc. 2011; 133:14098. [PubMed: 21797210]
30. Howerton BS, Heidary DK, Glazer EC. J Am Chem Soc. 2012; 134:8324. [PubMed: 22553960]
31. Shi G, Monro S, Hennigar R, Colpitts J, Fong J, Kasimova K, Yin H, DeCoste R, Spencer C, Chamberlain L, Mandel A, Lilge L, McFarland SA. Coord Chem Rev. 2015; 282–283:127.

32. Loftus LM, White JK, Albani BA, Kohler L, Kodanko JJ, Thummel RP, Dunbar KR, Turro C. Chem - Eur J. 2016; 22:3704. [PubMed: 26715085]
33. Campagna, S., Puntoriero, F., Nastasi, F., Bergamini, G., Balzani, V. Photochemistry and Photophysics of Coordination Compounds: Ruthenium. In: Balzani, V., Campagna, S., editors. Photochemistry and Photophysics of Coordination Compounds I. Vol. 280. Springer-Verlag; Berlin: 2007. p. 117-214.Topics in Current Chemistry
34. Malouf G, Ford PC. J Am Chem Soc. 1974; 96:601.
35. Caspar JV, Meyer TJ. Inorg Chem. 1983; 22:2444.
36. Durham B, Caspar JV, Nagle JK, Meyer TJ. J Am Chem Soc. 1982; 104:4803.
37. Durham B, Walsh JL, Carter CL, Meyer TJ. Inorg Chem. 1980; 19:860.
38. Allen GH, White RP, Rillema DP, Meyer TJ. J Am Chem Soc. 1984; 106:2613.
39. Wacholtz WM, Auerbach RA, Schmehl RH, Ollino M, Cherry WR. Inorg Chem. 1985; 24:1758.
40. Sun Q, Mosquera-Vazquez S, Suffren Y, Hankache J, Amstutz N, Daku LML, Vauthey E, Hauser A. Coord Chem Rev. 2015; 282–283:87.
41. Van Houten J, Watts RJ. J Am Chem Soc. 1976; 98:4853.
42. Wagenknecht PS, Ford PC. Coord Chem Rev. 2011; 255:591.
43. Tfouni E. Coord Chem Rev. 2000; 196:281.
44. Sun Q, Mosquera-Vazquez S, Daku LML, Guénée L, Goodwin HA, Vauthey E, Hauser A. J Am Chem Soc. 2013; 135:13660. [PubMed: 24000998]
45. Malouf G, Ford PC. J Am Chem Soc. 1977; 99:7213.
46. Tfouni E, Ford PC. Inorg Chem. 1980; 19:72.
47. Henderson LJ Jr, Fronczek FR, Cherry WR. J Am Chem Soc. 1984; 106:5876.
48. White JK, Schmehl RH, Turro C. Inorg Chim Acta. 2017; 454:7.
49. Wacholtz WF, Auerbach RA, Schmehl RH. Inorg Chem. 1986; 25:227.
50. Ross HB, Boldaji M, Rillema DP, Blanton CB, White RP. Inorg Chem. 1989; 28:1013.
51. Pinnick DV, Durham B. Inorg Chem. 1984; 23:1440.
52. Juris A, Balzani V, Barigelletti F, Campagna S, Belser P, von Zelewsky A. Coord Chem Rev. 1988; 84:85.
53. Van Houten J, Watts RJ. Inorg Chem. 1978; 17:3381.
54. Porter GB, Sparks RH. J Photochem. 1980; 13:123.
55. Tachiyashiki S, Mizumachi K. Coord Chem Rev. 1994; 132:113.
56. Sharma R, Knoll JD, Martin PD, Podgorski I, Turro C, Kodanko JJ. Inorg Chem. 2014; 53:3272. [PubMed: 24661182]
57. Li A, White JK, Arora K, Herroon MK, Martin PD, Schlegel HB, Podgorski I, Turro C, Kodanko JJ. Inorg Chem. 2016; 55:10. [PubMed: 26670781]
58. Sharma R, Knoll JD, Ancona N, Martin PD, Turro C, Kodanko JJ. Inorg Chem. 2015; 54:1901. [PubMed: 25611351]
59. Tu YJ, Mazumder S, Endicott JF, Turro C, Kodanko JJ, Schlegel HB. Inorg Chem. 2015; 54:8003. [PubMed: 26244447]
60. Chen, G., Crawford, J., Skerlj, R. Methods of Making 2,6-Diaryl Piperidine Derivatives. US Patent Appl. US 20050154201. Jun 14. 2005
61. Mikata Y, Yamanaka A, Yamashita A, Yano S. Inorg Chem. 2008; 47:7295. [PubMed: 18642899]
62. SAINT. Bruker AXS Inc; Madison, WI: 2012.
63. Sheldrick, GM. SADABS. University of Göttingen; Göttingen, Germany: 1996.
64. Dolomanov OV, Bourhis LJ, Gildea RJ, Howard JAK, Puschmann H. J Appl Crystallogr. 2009; 42:339.
65. Sheldrick GM. Acta Crystallogr, Sect A: Found Crystallogr. 2008; A64:112.
66. Sheldrick GM. Acta Crystallogr, Sect C: Struct Chem. 2015; C71:3.
67. Sheldrick GM. Acta Crystallogr, Sect A: Found Adv. 2015; A71:3.
68. Montalti, M., Credi, A., Prodi, L., Gandolfi, MT. Handbook of Photochemistry. 3. CRC Press; Boca Raton, FL: 2006. Chemical Actinometry; p. 601-616.

69. Frisch, MJ., Trucks, GW., Schlegel, HB., Scuseria, GE., Robb, MA., Cheeseman, JR., Scalmani, G., Barone, V., Mennucci, B., Petersson, GA., Nakatsuji, H., Caricato, M., Li, X., Hratchian, HP., Izmaylov, AF., Bloino, J., Zheng, G., Sonnenberg, JL., Hada, M., Ehara, M., Toyota, K., Fukuda, R., Hasegawa, J., Ishida, M., Nakajima, T., Honda, Y., Kitao, O., Nakai, H., Vreven, T., Montgomery, JA., Jr, Peralta, JE., Ogliaro, F., Bearpark, M., Heyd, JJ., Brothers, E., Kudin, KN., Staroverov, VN., Keith, T., Kobayashi, R., Normand, J., Raghavachari, K., Rendell, A., Burant, JC., Iyengar, SS., Tomasi, J., Cossi, M., Rega, N., Millam, JM., Klene, M., Knox, JE., Cross, JB., Bakken, V., Adamo, C., Jaramillo, J., Gomperts, R., Stratmann, RE., Yazyev, O., Austin, AJ., Cammi, R., Pomelli, C., Ochterski, JW., Martin, RL., Morokuma, K., Zakrzewski, VG., Voth, GA., Salvador, P., Dannenberg, JJ., Dapprich, S., Daniels, AD., Farkas, O., Foresman, JB., Ortiz, JV., Cioslowski, J., Fox, DJ. Gaussian 09, revision E01. Gaussian, Inc; Wallingford, CT: 2013.
70. Andrae D, Häußermann U, Dolg M, Stoll H, Preuß H. Theor Chim Acta. 1990; 77:123.
71. Schäfer A, Huber C, Ahlrichs R. J Chem Phys. 1994; 100:5829.
72. Perdew JP, Burke K, Ernzerhof M. Phys Rev Lett. 1996; 77:3865. [PubMed: 10062328]
73. Perdew JP, Burke K, Ernzerhof M. Phys Rev Lett. 1997; 78:1396.
74. Becke AD. J Chem Phys. 1993; 98:1372.
75. Lee C, Yang W, Parr RG. Phys Rev B: Condens Matter Mater Phys. 1988; 37:785.
76. Miehlich B, Savin A, Stoll H, Preuss H. Chem Phys Lett. 1989; 157:200.
77. Tomasi J, Mennucci B, Cammi R. Chem Rev. 2005; 105:2999. [PubMed: 16092826]
78. Dapprich S, Frenking G. J Phys Chem. 1995; 99:9352.
79. Gorelsky SI, Ghosh S, Solomon EI. J Am Chem Soc. 2006; 128:278. [PubMed: 16390158]
80. Gorelsky, SI. AOMix: Program for Molecular Orbital Analysis, version 6.85. 2015. http://www.sg-chem.net/
81. Gorelsky SI, Lever ABP. J Organomet Chem. 2001; 635:187.
82. Gorelsky SI, Basumallick L, Vura-Weis J, Sarangi R, Hodgson KO, Hedman B, Fujisawa K, Solomon EI. Inorg Chem. 2005; 44:4947. [PubMed: 15998022]
83. Gorelsky SI, Solomon EI. Theor Chem Acc. 2008; 119:57.
84. Burdzinski G, Hackett JC, Wang J, Gustafson TL, Hadad CM, Platz MS. J Am Chem Soc. 2006; 128:13402. [PubMed: 17031952]
85. Nakayama T, Amijima Y, Ibuki K, Hamanoue K. Rev Sci Instrum. 1997; 68:4364.
86. Marcu, L.French, PMW., Elson, DS., editors. Fluorescence Lifetime Spectroscopy and Imaging: Principles and Applications in Biomedical Diagnostics. CRC Press; Boca Raton, FL: 2014.
87. Kojima T, Amano T, Ishii Y, Ohba M, Okaue Y, Matsuda Y. Inorg Chem. 1998; 37:4076. [PubMed: 11670527]
88. Heeg MJ, Kroener R, Deutsch E. Acta Crystallogr, Sect C: Cryst Struct Commun. 1985; C41:684.
89. Hitchcock PB, Seddon KR, Turp JE, Yousif YZ, Zora JA, Constable EC, Wernberg O. J Chem Soc, Dalton Trans. 1988:1837.
90. Liu Y, Turner DB, Singh TN, Angeles-Boza AM, Chouai A, Dunbar KR, Turro C. J Am Chem Soc. 2009; 131:26. [PubMed: 19072048]
91. Knoll JD, Albani BA, Durr CB, Turro C. J Phys Chem A. 2014; 118:10603. [PubMed: 25027458]
92. Bridgeman AJ, Cavigliasso G, Ireland LR, Rothery J. J Chem Soc Dalt Trans. 2001:2095.
93. Bridgeman AJ. J Chem Soc, Dalton Trans. 1996:2601.
94. Bridgeman AJ. J Chem Soc, Dalton Trans. 1997:4765.
95. Bridgeman AJ, Bridgeman CH. Chem Phys Lett. 1997; 272:173.
96. Bridgeman AJ, Rothery J. J Chem Soc Dalt Trans. 2000:211.
97. Fillman KL, Przyojski JA, Al-Afyouni MH, Tonzetich ZJ, Neidig ML. Chem Sci. 2015; 6:1178. [PubMed: 25621143]
98. Harada T, Wada S, Yuge H, Miyamoto TK. Acta Crystallogr, Sect C: Cryst Struct Commun. 2003; C59:m37.
99. Galardon E, Le Maux P, Toupet L, Simonneaux G. Organometallics. 1998; 17:565.
100. Johnson BA, Agarwala H, White TA, Mijangos E, Maji S, Ott S. Chem - Eur J. 2016; 22:14870. [PubMed: 27459316]

101. Da Silva ACH, Da Silva JLF, Franco DW. Dalt Trans. 2016; 45:4907.
102. (a) Bhasikuttan AC, Suzuki M, Nakashima S, Okada T. J Am Chem Soc. 2002; 124:8398. [PubMed: 12105921] (b) Sun Y, Liu Y, Turro CJ. Am Chem Soc. 2010; 132:5594.
103. Cannizzo A, Van Mourik F, Gawelda W, Zgrablic G, Bressler C, Chergui M. Angew Chem, Int Ed. 2006; 45:3174.
104. Damrauer NH, Cerullo G, Yeh A, Boussie TR, Shank CV, McCusker JK. Science. 1997; 275:54. [PubMed: 8974388]
105. Borfecchia E, Garino C, Gianolio D, Salassa L, Gobetto R, Lamberti C. Catal Today. 2014; 229:34.
106. Borfecchia E, Garino C, Salassa L, Ruiu T, Gianolio D, Zhang X, Attenkofer K, Chen LX, Gobetto R, Sadler PJ, Lamberti C. Dalt Trans. 2013; 42:6564.
107. Greenough SE, Roberts GM, Smith NA, Horbury MD, McKinlay RG, Żurek JM, Paterson MJ, Sadler PJ, Stavros VG. Phys Chem Chem Phys. 2014; 16:19141. [PubMed: 25060066]

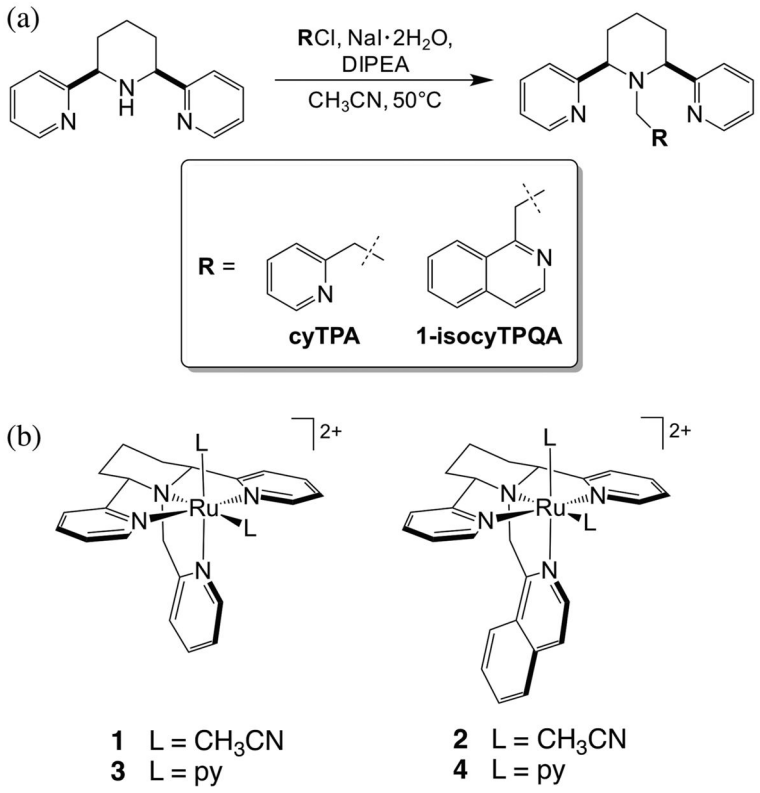

Figure 1.

(a) Synthetic route of the ligands cyTPA and 1-isocyTPQA and (b) molecular structures of complexes **1–4**.

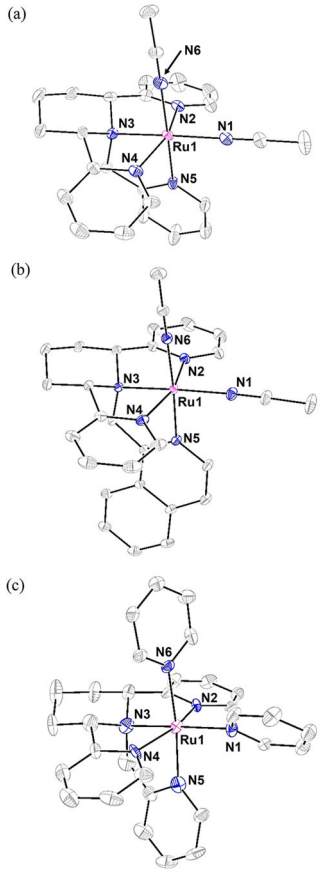

Figure 2.

ORTEP diagrams of the dications (a) **1** $[Ru(cyTPA)\text{-}(CH_3CN)_2]^{2+}$, (b) **2** $[Ru(1\text{-}isocyTPQA)(CH_3CN)_2]^{2+}$ and (c) **3** $[Ru(cyTPA)(py)_2]^{2+}$ (thermal ellipsoids shown at 50% probability, hydrogen atoms are omitted for clarity). Selected bond distances (Å) for **1**: Ru1–N1, 2.047(2); Ru1–N6, 2.047(2). Selected bond distances (Å) for **2**: Ru1–N1, 2.0312(8); Ru1–N6, 2.0331(8). Selected bond distances (Å) for **3**: Ru1–N1, 2.13(1); Ru1–N6, 2.12(1).

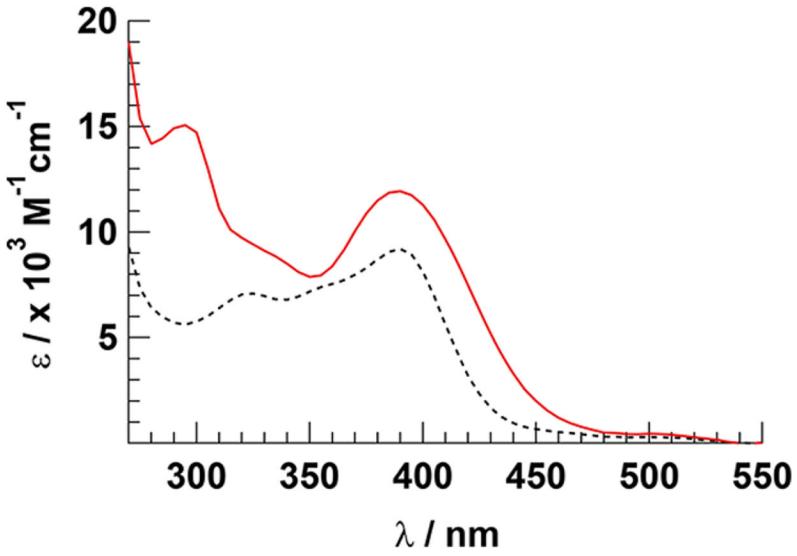

Figure 3.
Electronic absorption spectra of **1** (black, dashed) and **2** (red, solid) in DMSO.

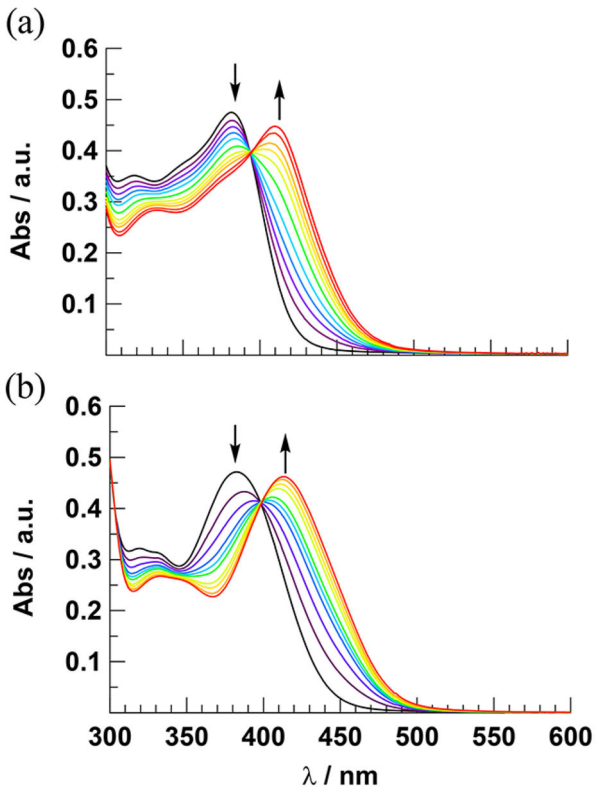

Figure 4.

Changes to the electronic absorption spectra upon irradiation ($\lambda_{irr} \geq 395$ nm) of (a) **1** (t_{irr} = 0–27 min) and (b) **2** (t_{irr} = 0–9 min) in H_2O (<5% acetone).

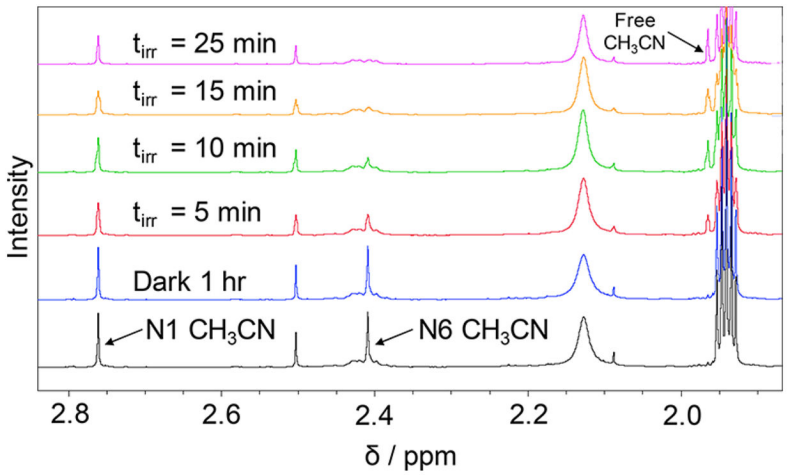

Figure 5.

Comparison of the aliphatic region of the ^{1}H NMR spectrum of **2** in CD_3CN as initially prepared in the dark (black), after 1 h in the dark (blue), and at various irradiation times (λ_{irr} ≥ 395 nm).

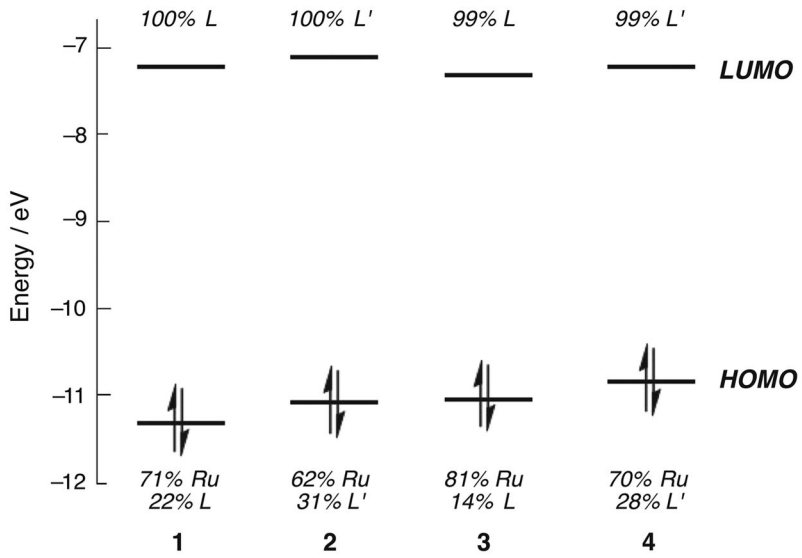

Figure 6.

Frontier molecular orbital diagram for complexes **1–4** in the ground state (L = cyTPA, L′ = 1-isocyTPQA).

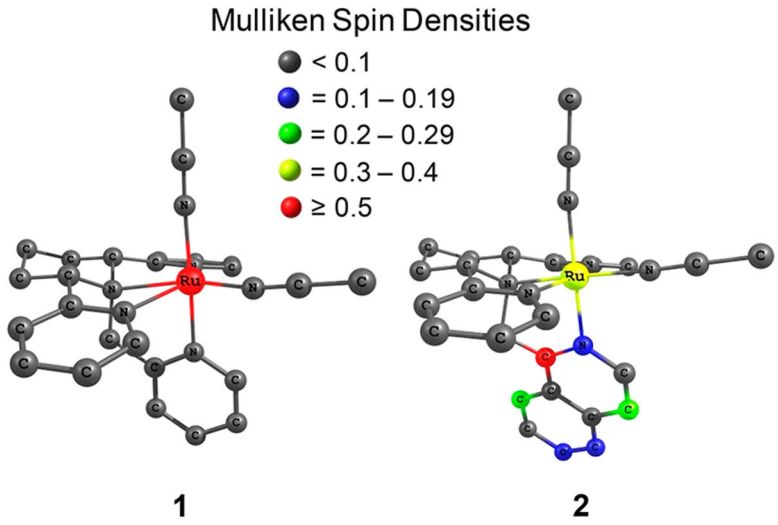

Figure 7.
Mulliken spin densities of the lowest energy triplet state calculated for **1** and **2**.

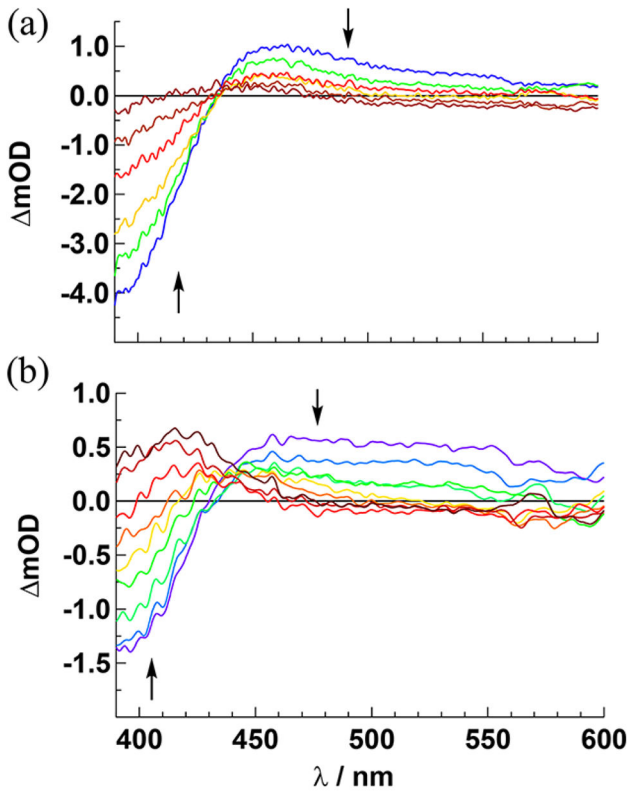

Figure 8.

Transient absorption spectra of **2** in (a) CH_3CN collected at 0.4, 8, 20, 51, 99, and 285 ps, and (b) acetone collected at 1, 3, 8, 17, 39 51, 192, 718, and 2681 ps following the laser pulse (λ_{exc} = 350 nm, fwhm = 85 fs, baseline collected at −20 ps).

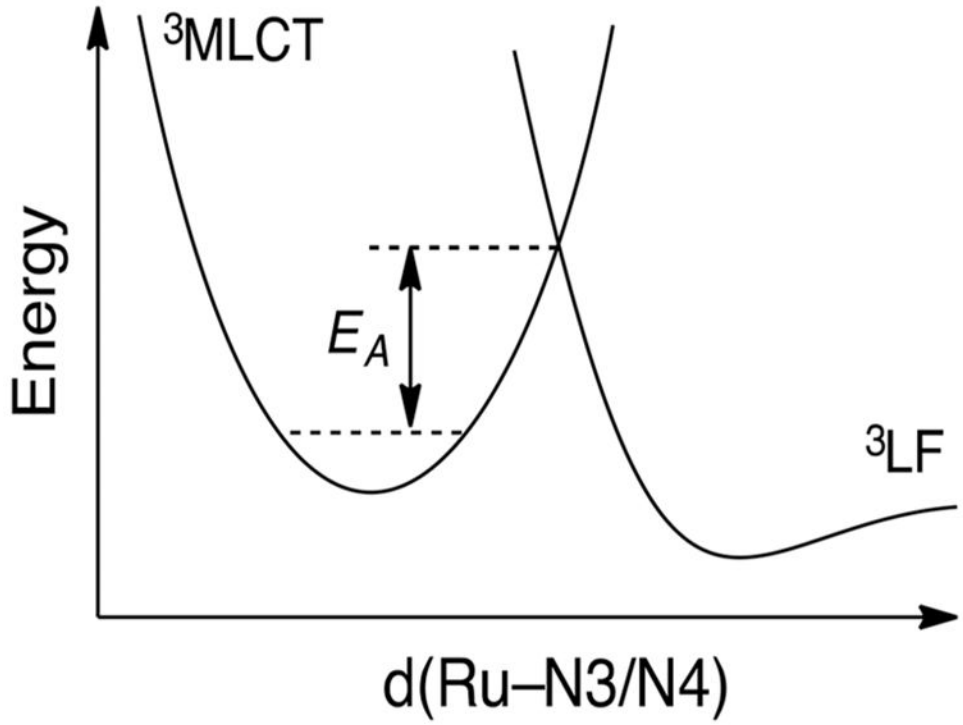

Figure 9.
Schematic representation of the relative energies of the ^{3}MLCT and ^{3}LF potential energy surfaces in **1**.

Table 1

Photochemical and Photophysical Data for 1–4

complex	Φ_{400}[a]	lowest ^{3}ES[b]	τ_{TA}/ps
1	0.0066(3)	^{3}LF	36[c]
2	0.033(3)	^{3}MLCT/$^3\pi\pi^*$	42[c]
3	0.0012(1)	^{3}LF	160[d]
4	0.0013(1)	^{3}LF	120[d]

[a] H_2O (<5% acetone) at 298 K.

[b] From Mulliken Spin Density Calculations.

[c] CH_3CN.

[d] Acetone.

Table 2

MBO Analysis for 1–4 in the Ground State Singlet and Lowest Energy Triplet State

	Ru–N6[a]		Ru–N5[b]	
complex	**singlet**	**triplet**	**singlet**	**triplet**
1	0.611	0.612	0.434	0.446
2	0.599	0.518	0.415	0.652
3	0.164	0.168	0.397	0.421
4	0.148	0.144	0.369	0.380

[a]N atom of CH_3CN in **1** and **2** and py in **3** and **4**.

[b]N atom of py arm of cyTPA in **1** and **3** and quinoline arm of 1-isocyTPQA in **2** and **4**.